Available online at www.sciencedirect.com
ScienceDirect
Journal of Computational Physics 227 (2008) 4459–4477
JOURNAL OF COMPUTATIONAL PHYSICS
www.elsevier.com/locate/jcp

Implicit spectrally-accurate method for moving boundary problems using immersed boundary conditions concept

S.Z. Husain, J.M. Floryan *

Department of Mechanical and Materials Engineering, The University of Western Ontario, London, Ontario, Canada N6A 5B9

Received 20 June 2007; received in revised form 27 December 2007; accepted 8 January 2008
Available online 15 January 2008

Abstract

A fully implicit, spectral algorithm for the analysis of moving boundary problem is described. The algorithm is based on the concept of immersed boundary conditions (IBC), i.e., the computational domain is fixed while the time dependent physical domain is submerged inside the computational domain, and is described in the context of the diffusion-type problems. The physical conditions along the edges of the physical domain are treated as internal constraints. The method eliminates the need for adaptive grid generation that follows evolution of the physical domain and provides sharp resolution of the location of the boundary. Various tests confirm the spectral accuracy in space and the first- and second-order accuracy in time. The computational cost advantage of the IBC method as compared with the more traditional algorithm based on the mapping concept is demonstrated.

Keywords: Immersed boundaries concept; Moving boundary problems; Spectral methods

1. Introduction

The term "moving boundary problem" refers to a problem where a boundary of the solution domain changes location during the solution process. The related problem where boundary motion is a priori unknown and has to be predicted as a part of the solution process is usually referred to as a free boundary problem. In the present work we are interested in finding a spectrally-accurate solution to the first problem that maintains sharp resolution of the location of the boundary.

Moving-boundary algorithms have been reviewed in Ref. [1] and can be classified as Eulerian, Lagrangian and mixed. Eulerian algorithms rely on a coordinate system that is stationary in a laboratory frame of reference or moves in a prescribed manner (Galileo transformation). Such algorithms can be divided for convenience into fixed grid methods, adaptive grid methods and various mapping methods.

* Corresponding author. Tel.: +1 519 661 2130; fax: +1 519 661 3757.
E-mail address: mfloryan@eng.uwa.ca (J.M. Floryan).

0021-9991/$ - see front matter © 2008 Elsevier Inc. All rights reserved.
doi:10.1016/j.jcp.2008.01.002

In the fixed grid methods the grid is fixed in the domain and, since in general, the location of the moving boundary does not overlap with a grid line, a special procedure must be added to identify location of the moving boundary. This location can be tracked using either surface or volume tracking procedures. In the former approach a set of points is introduced to mark location of the boundary which is represented as a set of interpolated curves. These points are moved in a prescribed manner during the solution process [2,6] and provide ability for precise identification of boundary location. In the latter approach the information about the boundary location is not stored but the boundary is reconstructed whenever necessary on the basis of the presence of certain quantity of a convenient marker within computational cell, e.g., MAC – Marker and Cell [3], VOF – Volume of Fluid [4,12] and Level Set [9,13] methods. The reconstruction process leads to a diffused location of the boundary but the overall accuracy can be made consistent with low accuracy discretization schemes for the field equations.

In the adaptive grid methods the computational grid is continuously adapted so that one of the grid lines always overlaps with the moving boundary. This leads to a large computational overhead associated with grid re-generation at each simulation time step. In this sense numerical grid generation combined with finite-difference discretization of the field equations and grid generation for the finite-element discretization are conceptually identical. In certain situations numerical grid generation can be replaced by analytical mappings, but this does not alter the basic concept of such methods. The overall accuracy of tracking of the location of the boundary is determined by the accuracy of numerical implementation of various mapping schemes.

Lagrangian methods are characterized by a coordinate system that moves with the fluid. Each computational cell always contains the same fluid and its tracking requires solution of an initial value problem. These methods are well suited for moving boundary problems as they permit simple delineation of moving boundaries. The two main problems involve mesh tangling and loss of numerical accuracy associated with highly distorted meshes. Possible remedies are discussed in Ref. [1]. Mixed Lagrangian–Eulerian methods rely on the combination of concepts described above [1].

The accuracy of the available methods for solving moving boundary problems is dictated by the accuracy of representation of boundary location and by the discretization error of the field equations. Spectral methods provide the lowest error for the field equations and thus are of interest in this work. The variability of geometry of the solution domain represents the main challenge for implementation of these methods. One possible implementation can be based on the use of the concept of immersed boundary conditions [11]. This concept has been proposed in Refs. [8,10] in the context of simulation of cardiac dynamics but its first spectrally-accurate implementation for fixed boundary problems has been given in Ref. [11]. Immersed boundary conditions method uses fixed, regular solution domain for the required spectral expansions and the actual physical domain is submerged in the interior of the computational domain. Boundary conditions at the edges of the physical domain are replaced by constraints imposed inside computational domain. The method is analogous to the fixed grid methods discussed above.

The present work describes extension of the algorithm proposed in Ref. [11] to the case of moving boundary problems. The analysis is carried out in the context of diffusion problem. The model problem is described in Section 2. The immersed boundary conditions (IBC) method is discussed in Section 3. The domain transformation (DT) method that is used to demonstrate the efficiency of the IBC method is discussed in Section 4. Results of numerical tests are discussed in Section 5. Section 6 provides a short summary of the main conclusions.

2. Model problem

We shall pose the problem of interest in the context of heat conduction. Consider unsteady conductive heat flow in a slot bounded by corrugated walls whose geometry changes as a function of time and is described by the following relations (see Fig. 1)

$$y_L(x,t) = -1 + \sum_{n=-\infty}^{\infty} H_L^{(n)}(t) e^{in\alpha x}, \quad y_U(x,t) = 1 + \sum_{n=-\infty}^{\infty} H_U^{(n)}(t) e^{in\alpha x}, \tag{2.1a, b}$$

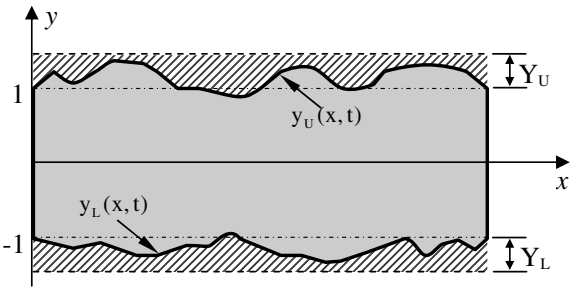

Fig. 1. Sketch of the instantaneous form of the domain of interest in the physical plane.

where $H_L^{(n)} = H_L^{(-n)*}$, $H_U^{(n)} = H_U^{(-n)*}$ and star denotes complex conjugate. Such problems are of interest in the case of nano-channels and nano-switches where the effects of surface roughness could be significant [7]. The slot is periodic with wavelength $\lambda = 2\pi/\alpha$ and extends to $\pm\infty$ in the x-direction. The dimensionless field equation describing heat flow has the form

$$\partial^2\theta/\partial x^2 + \partial^2\theta/\partial y^2 = \partial\theta/\partial t, \tag{2.2}$$

where θ denotes temperature. This equation needs to be supplemented by suitable initial and boundary conditions, which are taken to be in the form

$$\theta(x,y,t=0) = \theta_i, \quad y_L(x,0) = y_{Li}(x), \quad y_U(x,0) = y_{Ui}(x), \tag{2.3a–c}$$

$$\theta(x,y_L(x,t),t) = \theta_L(x,t), \quad \theta(x,y_U(x,t),t) = \theta_U(x,t), \tag{2.4a, b}$$

where θ_i, y_{Li}, y_{Ui}, θ_L, θ_U are considered to be known. The time variations of the temperature field result from the variations of the temperature along the edges of the physical domain as well as from the deformation of the domain. The main difficulty in finding a solution to (2.2)–(2.4) is associated with the variations of the geometry of the physical domain, which leads to the moving boundary problem. We shall discuss two solution methods suitable for this problem, i.e., a method based on the concept of immersed boundary conditions (IBC) and a method based on the concept of domain transformation (DT). The latter method will be used to illustrate advantages of the IBC method. We shall begin our discussion with the former method.

3. The immersed boundary conditions (IBC) method

We are interested in the determination of the solution of (2.2)–(2.4) with spectral accuracy. We shall use Fourier expansions in the x-direction and expansions in terms of Chebyshev polynomials in the y-direction. Standard definition of Chebyshev polynomials uses domain $(-1,1)$, however the physical domain is confined between $(1 + Y_U)$ and $(-1 - Y_L)$, where Y_U and Y_L denote the locations of extremities of the domain of interest during time interval of interest (see Fig. 1). The first step in the solution process involves a mapping from the physical (x, y) coordinates to the computational $(x,\hat{y})$ coordinates in the form

$$\hat{y} = 2\frac{y - (1 + Y_U)}{1 + Y_U - (-1 - Y_L)} + 1, \tag{3.1}$$

where $\hat{y} \in \langle -1, 1\rangle$. The governing equation takes the form

$$\partial^2\theta/\partial x^2 + \Gamma^2\partial^2\theta/\partial\hat{y}^2 = \partial\theta/\partial t \tag{3.2}$$

where $\Gamma = 2/(2 + Y_U + Y_L)$ is a constant. Locations of the corrugated boundaries in the $(x,\hat{y})$ plane are given as

$$\hat{y}_L(x,t) = \sum_{n=-\infty}^{\infty} A_L^{(n)}(t)e^{in\alpha x}, \quad \hat{y}_U(x,t) = \sum_{n=-\infty}^{\infty} A_U^{(n)}(t)e^{in\alpha x}, \tag{3.3a, b}$$

where $A_L^{(0)}(t) = 1 + \Gamma[-2 - Y_U + H_L^{(0)}(t)]$, $A_L^{(n)}(t) = \Gamma H_L^{(n)}(t)$ for $n \neq 0$, $A_U^{(0)}(t) = 1 + \Gamma[-Y_U + H_U^{(0)}(t)]$, $A_U^{(n)}(t) = \Gamma H_U^{(n)}(t)$ for $n \neq 0$. The boundary conditions at the transformed boundaries become

$$\theta(x,\hat{y}_{\mathrm{L}}(x,t),t)=\theta_{\mathrm{L}}(x,t),\quad \theta(x,\hat{y}_{\mathrm{U}}(x,t),t)=\theta_{\mathrm{U}}(x,t). \tag{3.4a, b}$$

The solution can be represented in the form of Fourier expansion

$$\theta(x,\hat{y},t)=\sum_{n=-\infty}^{\infty}\Phi^{(n)}(\hat{y},t)\mathrm{e}^{\mathrm{i}n\alpha x}\approx\sum_{n=-N_{\mathrm{M}}}^{N_{\mathrm{M}}}\Phi^{(n)}(\hat{y},t)\mathrm{e}^{\mathrm{i}n\alpha x}, \tag{3.5}$$

where $\Phi^{(n)}(\hat{y},t)=\Phi^{(-n)*}(\hat{y},t)$ and star denotes complex conjugate. Substitution of (3.5) into the field equation and separation of Fourier components lead to an uncoupled system of parabolic partial differential equations for $\Phi^{(n)}$, $n\in\langle 0,N_{\mathrm{M}}\rangle$, of the type

$$\partial\Phi^{(n)}/\partial t=(\Gamma^2D^2-n^2\alpha^2)\Phi^{(n)}, \tag{3.6}$$

where $D=d/d\hat{y}$. Two types of temporal discretizations are used. The two-step implicit method results in the following relations

$$[\Gamma^2D^2-(n^2\alpha^2+1.5\Delta t^{-1})]\Phi^{(n)}_{\tau+1}=-2\Delta t^{-1}\Phi^{(n)}_{\tau}+0.5\Delta t^{-1}\Phi^{(n)}_{\tau-1},n\in\langle 0,N_{\mathrm{M}}\rangle, \tag{3.7}$$

while similar relations resulting from the one-step, self-starting implicit method are shown in Appendix A. In the above the subscript, τ denotes the time step and Δt stands for the (constant) length of the time step. Relation (3.7) has the form of an inhomogeneous ordinary differential equation for $\Phi^{(n)}_{\tau+1}$. The following discussion will be carried out in the context of the two-step method, while the relevant relations for the one-step method can be readily deduced.

The unknown function $\Phi^{(n)}_{\tau+1}$ can be represented in terms of expansions based on Chebyshev polynomials in the form

$$\Phi^{(n)}_{\tau+1}(\hat{y})=\sum_{k=0}^{\infty}G^{(n)}_{k,\tau+1}T_k(\hat{y})\approx\sum_{k=0}^{N_{\mathrm{T}}}G^{(n)}_{k,\tau+1}T_k(\hat{y}), \tag{3.8}$$

where T_k denotes the Chebyshev polynomial of kth order and $G^{(n)}_{k,\tau+1}$ are the unknown coefficients of the expansion. Substitution of (3.8) into (3.7) gives

$$[\Gamma^2D^2-(n^2\alpha^2+1.5\Delta t^{-1})]\sum_{k=0}^{\infty}G^{(n)}_{k,\tau+1}T_k=-2\Delta t^{-1}\sum_{k=0}^{\infty}G^{(n)}_{k,\tau}T_k+0.5\Delta t^{-1}\sum_{k=0}^{\infty}G^{(n)}_{k,\tau-1}T_k. \tag{3.9}$$

We use Galerkin procedure to develop equations for the unknowns $G^{(n)}_{k,\tau+1}$, i.e., we multiply both sides of (3.9) by $T_j(\hat{y})$ and integrate with the weight function $\hat{\omega}=1/\sqrt{1-\hat{y}^2}$ to get

$$\begin{aligned}&\sum_{k=0}^{N_{\mathrm{T}}}[\Gamma^2\langle T_j,D^2T_k\rangle-(n^2\alpha^2+1.5\Delta t^{-1})\langle T_j,T_k\rangle]G^{(n)}_{k,\tau+1}\\&\quad=-2\Delta t^{-1}\sum_{k=0}^{N_{\mathrm{T}}}\langle T_j,T_k\rangle G^{(n)}_{k,\tau}+0.5\Delta t^{-1}\sum_{k=0}^{N_{\mathrm{T}}}\langle T_j,T_k\rangle G^{(n)}_{k,\tau-1},\quad j\in\langle 0,N_{\mathrm{T}}\rangle,\end{aligned} \tag{3.10}$$

where the inner product is defined as $\langle f_j(\hat{y}),g_k(\hat{y})\rangle=\int_{-1}^{1}f_j(\hat{y})g_k(\hat{y})\hat{\omega}(\hat{y})\mathrm{d}\hat{y}$. Evaluation of inner products can be significantly simplified by taking advantage of the well known orthogonality properties of the Chebyshev polynomials. Eq. (3.10) leads to $N_{\mathrm{T}}-1$ decoupled algebraic equations for each Fourier mode; two additional equations required in order to close the system need to be derived from the boundary conditions and these conditions provide coupling between different Fourier modes [5,11].

The boundary conditions are to be enforced along the lines $\hat{y}_{\mathrm{L}}(x,\tau+1)$ and $\hat{y}_{\mathrm{U}}(x,\tau+1)$ while the solution domain remains fixed at $\hat{y}\in\langle -1,1\rangle$. To explain the immersed boundary conditions method in general, at time $\tau+1$, we evaluate the unknown $\theta(x,\tau+1)\equiv\theta(x,f(x,\tau+1),\tau+1)$ along an arbitrary time dependent line that at time $t=\tau+1$ occupies position $y=f(x,\tau+1)$, such that f is a periodic function with period $\lambda=2\pi/\alpha$ and $|f(x,\tau+1)|\leqslant 1$. The function $f(x,\tau+1)$ can be expressed without losing generality as

$$f(x,\tau+1)=\sum_{n=-\infty}^{\infty}P^{(n)}_{\tau+1}\mathrm{e}^{\mathrm{i}n\alpha x}\approx\sum_{n=-N_A}^{N_A}P^{(n)}_{\tau+1}\mathrm{e}^{\mathrm{i}n\alpha x}, \tag{3.11}$$

where one in practice deals with a finite number of terms N_A. The unknown $\theta_l(x,\tau+1)$ is periodic in x with the same period λ and thus can be expressed in terms of Fourier series as

$$\theta_l(x,\tau+1) \equiv \theta(x,f(x,\tau+1),\tau+1) = \sum_{n=-N_\theta}^{N_\theta} \varphi_{\tau+1}^{(n)} e^{in\alpha x}, \tag{3.12}$$

where $N_\theta = N_T N_A + N_M$. Since the flow representation is limited to $N_M + 1$ modes, we will be able to enforce constraints only on the first $(N_M + 1)$ terms in (3.12). The same unknown can be expressed using the discretized form of the solution, i.e.,

$$\theta_l(x,\tau+1) = \sum_{n=-N_M}^{N_M} \Phi^{(n)}(f(x,\tau+1),\tau+1) e^{in\alpha x} = \sum_{n=-N_M}^{N_M} \sum_{k=0}^{N_T} G_{k,\tau+1}^{(n)} T_k(f(x,\tau+1)) e^{in\alpha x}. \tag{3.13}$$

Since $T_k(f(x,\tau+1))$ is periodic in x, it can be expressed in terms of Fourier expansion as follows:

$$T_k(f(x,\tau+1)) = \sum_{m=-\infty}^{\infty} w_{k,\tau+1}^{(m)} e^{im\alpha x}. \tag{3.14}$$

The expansion coefficients in (3.14) can be evaluated with the help of the recurrence relation for Chebyshev polynomials in the form $T_{k+1}(\hat{y}) = 2\hat{y}T_k(\hat{y}) - T_{k-1}(\hat{y})$ that leads to the following recurrence relation

$$w_{k+1,\tau+1}^{(m)} = 2\sum_{n=-\infty}^{\infty} P_{\tau+1}^{(n)} w_{k,\tau+1}^{(m-n)} - w_{k-1,\tau+1}^{(m)} \tag{3.15}$$

whose evaluation begins at $k = 0$ and results in

$$w_{0,\tau+1}^{(0)} = 1, \quad w_{0,\tau+1}^{(m)} = 0 \quad \text{for } |m| \geqslant 1; \quad w_{1,\tau+1}^{(m)} = P_{\tau+1}^{(m)} \quad \text{for } |m| \geqslant 0. \tag{3.16}$$

Substitution of (3.14) into (3.13) gives

$$\theta_l(x,\tau+1) = \sum_{n=-N_M}^{N_M} \sum_{k=0}^{N_T} \sum_{m=-\infty}^{\infty} G_{k,\tau+1}^{(n)} w_{k,\tau+1}^{(m)} e^{i(n+m)\alpha x} = \sum_{n=-\infty}^{\infty} \sum_{m=-N_M}^{N_M} \sum_{k=0}^{N_T} G_{k,\tau+1}^{(m)} w_{k,\tau+1}^{(n-m)} e^{in\alpha x} \tag{3.17}$$

and comparison of (3.12) with (3.17) gives

$$\varphi_{\tau+1}^{(n)} = \sum_{m=-N_M}^{N_M} \sum_{k=0}^{N_T} G_{k,\tau+1}^{(m)} w_{k,\tau+1}^{(n-m)}. \tag{3.18}$$

Eq. (3.18) can be used to express boundary conditions along the lines $\hat{y}_L(x,\tau+1)$ and $\hat{y}_U(x,\tau+1)$. In the case of our model problem these boundary conditions take the following form

$$\sum_{m=-N_M}^{N_M} \sum_{k=0}^{N_T} G_{k,\tau+1}^{(m)} (w_L)_{k,\tau+1}^{(n-m)} = \Phi_{L,\tau+1}^{(n)} \qquad \sum_{m=-N_M}^{N_M} \sum_{k=0}^{N_T} G_{k,\tau+1}^{(m)} (w_U)_{k,\tau+1}^{(n-m)} = \Phi_{U,\tau+1}^{(n)}, \tag{3.19a, b}$$

where $\theta_L(x,\tau+1) = \sum_{n=-N_M}^{N_M} \Phi_{L,\tau+1}^{(n)} e^{in\alpha x}$, $\theta_U(x,\tau+1) = \sum_{n=-N_M}^{N_M} \Phi_{U,\tau+1}^{(n)} e^{in\alpha x}$ and (3.19a,b) corresponds to the lower and upper walls, respectively. Eqs. (3.10) and (3.19) form a complete set of algebraic equations for the unknown coefficients $G_{k,\tau+1}^{(n)}, k = 0,\ldots,N_T, n = 0,\ldots,N_M$. A direct solution of this system moves simulations by one time step forward and the resulting algorithm will be referred to as the direct algorithm.

In the case of time steps of constant length, the coefficients of the discretized equation (3.10) do not depend on time and thus this part of the coefficient matrix need to be constructed only once at the beginning of the solution process. The matrix entries corresponding to the boundary conditions (3.19) need to be reconstructed at every step of the simulations process; the reader should note that this is where the information about the motion of the boundaries enters into considerations.

The matrix of coefficients can be very large when a large number of Fourier modes are required and this motivates the search for an efficient solution method. Before solution is to be carried out the matrix is reduced to a real form by taking advantage of the complex conjugate properties $\Phi^{(n)}(\hat{y},t) = \Phi^{(-n)*}(\hat{y},t)$ (see Eq. (3.5)) resulting in a structure shown in Fig. 2 where the horizontal lines show the coupling effect of boundary

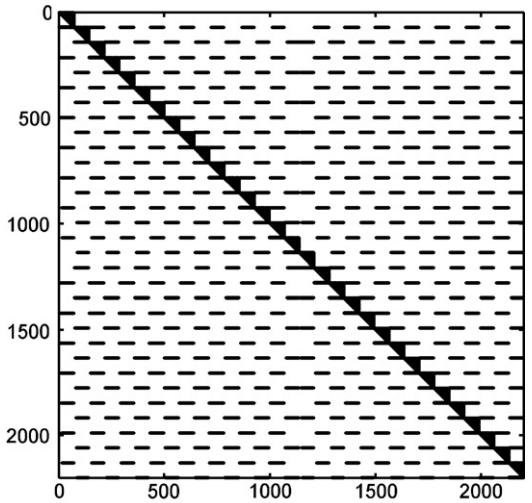

Fig. 2. Structure of the coefficient matrix resulting from the implementation of the immersed boundary condition method for $N_M = 15$ and $N_T = 70$ and the test problem (5.7)–(5.8). Only non-zero elements are marked.

conditions (3.19) and the blocks of coefficients in the upper triangular form resulting from the discretization of the differential Eq. (3.6) form a band along the diagonal. Such structure suggests the use of an iterative solution algorithm based on the decoupling of Fourier modes. The unknowns corresponding to a Fourier mode of interest in Eq. (3.19) at the current time step can be expressed in terms of the remaining Fourier modes using their values from the previous time step (or from the previous iteration). The solution process begins with mode 0, proceeds to the next mode using the most recent information available and continues until the last mode N_M is reached, and then it is repeated until a convergence criterion is satisfied. In this way, the solution of the complete system of size $(N_T + 1)^*(2N_M + 1)$ is replaced by a repetitive solution of systems of $(N_T + 1)$ equations for each Fourier mode. The rate of convergence is generally very good; it decreases with an increase of the current amplitude and the wave number characterizing wall geometry. We shall refer to the iterative algorithm as the "decoupled algorithm" and discuss performance of its various variants in Section 5. We wish to stress at this moment that the use of the decoupled algorithm significantly reduces memory requirements as one needs to work with many small matrices instead of one very large matrix as well as it opens the possibility for parallelization of the computations. This issue becomes significant in the case of three-dimensional problems and large number of Fourier modes and Chebyshev polynomials.

4. The domain transformation (DT) method

A very popular approach in dealing with moving boundary problems involves adjusting grid so that one of the grid lines always overlaps with the instantaneous location of the boundary [1]. The adjustments may have many forms, extending from analytical mappings to numerical coordinate generation. The adjustments in the shape of elements in the finite element method can also be viewed as a form of mapping. In order to judge the efficiency of the IBC method as compared to all other mapping-type methods, we selected the simplest method that relies on analytical mapping. The current shape of the slot in the physical domain (x, y) is mapped into a straight slot in the computational domain (ξ, η) with $\eta \in \langle -1, 1 \rangle$ using mapping in the form

$$\xi = x, \qquad \eta = 2\frac{(y - y_U(x,t))}{y_U(x,t) - y_L(x,t)} + 1. \tag{4.1}$$

After mapping Eq. (2.1) takes the form

$$\frac{\partial^2\theta}{\partial\eta^2} + W_1(\xi,\eta,t)\frac{\partial\theta}{\partial\eta} + W_2(\xi,\eta,t)\frac{\partial^2\theta}{\partial\xi\partial\eta} + W_3(\xi,\eta,t)\frac{\partial^2\theta}{\partial\xi^2} = W_3(\xi,\eta,t)\frac{\partial\theta}{\partial t}, \tag{4.2}$$

where $W_1(\xi,\eta,t) = (\eta_{xx} - \eta_t)/(\eta_x^2 + \eta_y^2)$, $W_2(\xi,\eta,t) = 2\eta_x/(\eta_x^2 + \eta_y^2)$ and $W_3(\xi,\eta,t) = 1/(\eta_x^2 + \eta_y^2)$. Expressions for η_t, η_x, η_{xx} and η_y are given in Appendix B. Solution of (4.2) is represented in terms of Fourier expansion as

$$\theta(\xi,\eta,t) = \sum_{n=-\infty}^{\infty} \Psi^{(n)}(\eta,t)\mathrm{e}^{\mathrm{i}n\alpha\xi} \approx \sum_{n=-N_M}^{N_M} \Psi^{(n)}(\eta,t)\mathrm{e}^{\mathrm{i}n\alpha\xi}, \tag{4.3}$$

where $\Psi^{(n)} = \Psi^{(-n)*}$ and the known coefficients W_1, W_2 and W_3 at each time $t = \tau$ are replaced by their Fourier expansions

$$W_1(\xi,\eta,\tau) = \sum_{m=-2N_M}^{2N_M} w_{1,\tau}^{(m)}(\eta)\mathrm{e}^{\mathrm{i}m\alpha\xi}, \quad W_2(\xi,\eta,\tau) = \sum_{m=-2N_M}^{2N_M} w_{2,\tau}^{(m)}(\eta)\mathrm{e}^{\mathrm{i}m\alpha\xi},$$
$$W_3(\xi,\eta,\tau) = \sum_{m=-2N_M}^{2N_M} w_{3,\tau}^{(m)}(\eta)\mathrm{e}^{\mathrm{i}m\alpha\xi}. \tag{4.4}$$

Substitution of (4.3) and (4.4) into (4.2), separation of Fourier components and the use of a two-step implicit method for the temporal discretization leads to

$$D^2\Psi_{\tau+1}^{(n)} + \sum_{s=-N_M}^{N_M} [w_{1,\tau+1}^{(n-s)} + \mathrm{i}s\alpha w_{2,\tau+1}^{(n-s)}]D\Psi_{\tau+1}^{(s)} - \sum_{s=-N_M}^{N_M} [(s\alpha)^2 + 1.5\Delta t^{-1}]w_{3,\tau+1}^{(n-s)}\Psi_{\tau+1}^{(s)}$$
$$= -2\Delta t^{-1}\sum_{s=-N_M}^{N_M} w_{3,\tau}^{(n-s)}\Psi_{\tau}^{(s)} + 0.5\Delta t^{-1}\sum_{s=-N_M}^{N_M} w_{3,\tau-1}^{(n-s)}\Psi_{\tau-1}^{(s)}, \quad n \in \langle 0, N_M\rangle \tag{4.5}$$

where $D = \mathrm{d}/\mathrm{d}\eta$. A similar expression for the one-step implicit method can be found in Appendix A. The reader may note that all Eq. (4.5) are coupled together through the known variable coefficients. The unknown $\Psi_{\tau+1}^{(n)}(\eta)$ can be expressed with spectral accuracy using the Chebyshev expansion in the form

$$\Psi_{\tau+1}^{(n)}(\eta) = \sum_{k=0}^{\infty} F_{k,\tau+1}^{(n)} T_k(\eta) \approx \sum_{k=0}^{N_T} F_{k,\tau+1}^{(n)} T_k(\eta). \tag{4.6}$$

Use of the Galerkin procedure described in Section 3 lead to $N_T - 1$ algebraic equations for $F_{k,\tau+1}^{(n)}$ for each Fourier mode. The remaining closing conditions come from the boundary conditions.

The treatment of boundary conditions follows standard procedures. The boundary conditions have the form

$$\theta(\xi,\eta=-1,t) = \theta_L(\xi,t) = \sum_{n=-N_M}^{N_M} \Psi_L^{(n)}(t)\mathrm{e}^{\mathrm{i}n\alpha\xi}, \quad \theta(\xi,\eta=1,t) = \theta_U(\xi,t) = \sum_{n=-N_M}^{N_M} \Psi_U^{(n)}(t)\mathrm{e}^{\mathrm{i}n\alpha\xi}. \tag{4.7a, b}$$

Use of (4.3) leads to the boundary conditions for each Fourier mode in the form

$$\Psi^{(n)}(-1,t) = \Psi_L^{(n)}(t), \quad \Psi^{(n)}(1,t) = \Psi_U^{(n)}(t). \tag{4.8a, b}$$

Introduction of Chebyshev expansion (4.6) leads to the required closing conditions in the form

$$\sum_{k=0}^{N_T}(-1)^k F_{k,\tau+1}^{(n)} = \Psi_{L,\tau+1}^{(n)}, \quad \sum_{k=0}^{N_T} F_{k,\tau+1}^{(n)} = \Psi_{U,\tau+1}^{(n)}. \tag{4.9a, b}$$

The above process leads to a system of equations with a full matrix of coefficients. Solution of this system moves simulations by one time step forward and this approach has been referred to in the previous section as the direct algorithm. As the matrix is full, no special iterative algorithm can be proposed. All entries corresponding to differential equation (4.5) need to be reconstructed at each time step while entries corresponding to boundary conditions remain essentially unchanged, which is opposite to what had to be done in the case of the IBC method. This observation suggests that the IBC method could be significantly faster when the cost of construction of the coefficient matrix is significant. This issue will be discussed in the next section.

5. Testing of the algorithms

We shall discuss performance of the algorithms in the context of two convenient test problems involving movements of boundaries, i.e., movements of the upper wall corresponding (i) to an elastic traveling wave and (ii) to a standing elastic wave.

5.1. Elastic traveling wave

Consider an elastic wave traveling along the upper wall with the lower wall being flat. The shape of the resulting slot can be described as

$$y_U(x,t) = 1 + S\cos[\alpha(x - ct)], \quad y_L = -1. \tag{5.1}$$

where c denotes the phase speed, α denotes the wave number and S stands for the amplitude of the wave. Time variations of the shape of the slot are illustrated in Fig. 3. We wish to determine variations of the temperature in the interior of the slot while keeping the temperature of the upper wall at $\theta_U = 0$ and at the lower wall at $\theta_L = 1$. Use of the Galileo transformation

$$X = x - ct \tag{5.2}$$

transforms the unsteady moving boundary problem into a steady fixed boundary problem with a sinusoidal upper wall. The full problem in the moving frame of reference (X, y) has the form

$$\partial^2\theta/\partial X^2 + c\partial\theta/\partial X + \partial^2\theta/\partial y^2 = 0 \tag{5.3}$$

with boundary conditions in the form

$$\theta(X,-1) = 1, \quad \theta(y_U(X)) = 0 \quad \text{where } y_U = 1 + S\cos(\alpha X). \tag{5.4}$$

Problem (5.3)–(5.4) is solved using IBC method and its performance can be judged by determining the character of the error. Error variations as a function of the number of Chebyshev polynomials N_T and Fourier modes N_M used in the computations have been analyzed where the reference solution obtained with $N_T = 100$ and $N_M = 25$ (these parameters provide machine level accuracy) played the role of a benchmark. In the y-direction, the Chebyshev expansions (3.8) with coefficients calculated using Galerkin procedure (3.10) are guaranteed to be spectrally-accurate with the increasing number of terms N_T. The error produced even with $N_T = 30$ polynomials was so small that it was not possible to follow its evolution using 64 bit arithmetic. Exponential decrease of the error as a function of N_M is documented in Fig. 4. Distribution of the error in the slot displayed in Fig. 5 demonstrates that the maximum of the error occurs at the corrugated boundary. The error of spatial discretization can thus be judged by looking only at the error of enforcement of boundary conditions at the upper wall. For convenience, we use the L_∞ norm for θ evaluated at the upper wall defined as

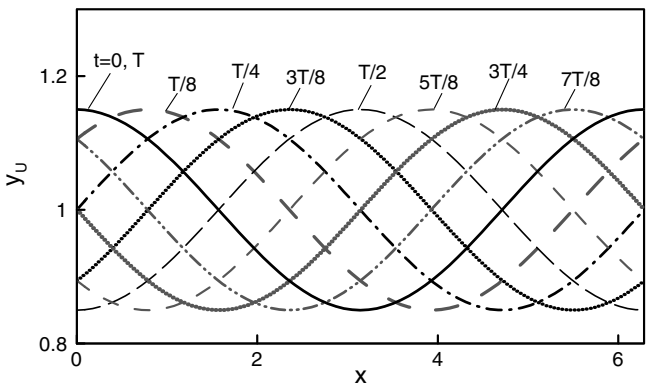

Fig. 3. Shape of the upper wall deformed by elastic traveling wave described by Eq. (5.1) with the amplitude $S = 0.15$, the wavenumber $\alpha = 1.0$ and the phase speed $c = \pi$ at $t = 0, T/8, T/4, 3T/8, T/2, 5T/8, 3T/4, 7T/8$ and T, where T denotes one time period.

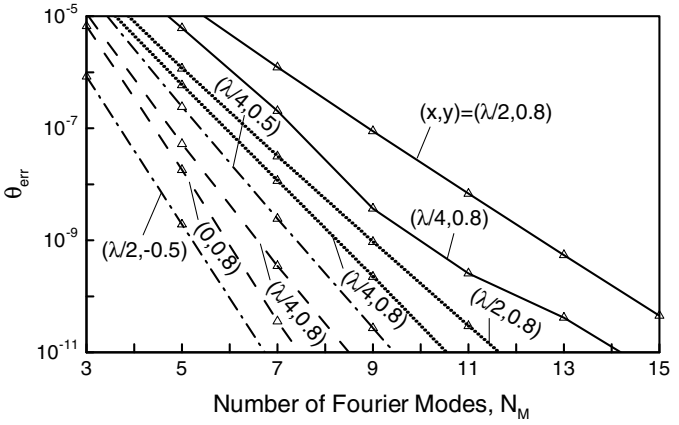

Fig. 4. Variations of the error at several test points in the interior of the solution domain as a function of the number of Fourier modes N_M used in the computations for the model problem (5.3)–(5.4) with $c = \pi$. The dashed-lines correspond to $S = 0.1$ and $\alpha = 1.0$, the dash-dotted-lines correspond to $S = 0.15$ and $\alpha = 1.0$, the dotted-lines correspond to $S = 0.1$ and $\alpha = 2.0$, and the solid-lines correspond to $S = 0.15$ and $\alpha = 2.0$. $N_T = 100$ Chebyshev polynomials were used in the computations. Error is defined as the absolute difference between the current results and the reference solution obtained using $N_M = 25$ Fourier modes and $N_T = 100$ Chebyshev polynomials at the same locations (the reference solution provides machine level accuracy).

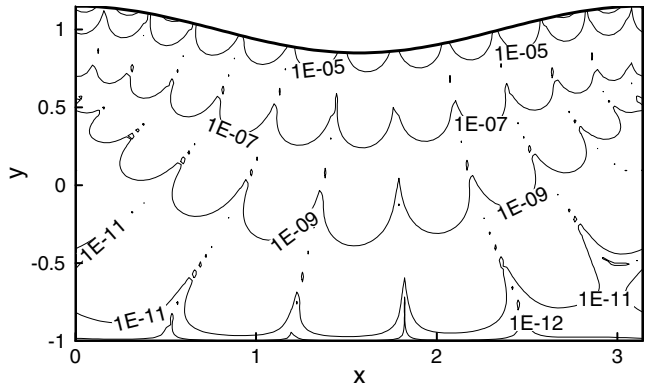

Fig. 5. Distribution of the error of the solution of the model problem (5.3)–(5.4) with the amplitude $S = 0.15$, the wave number $\alpha = 2.0$ and the phase speed $c = \pi$ determined using $N_M = 5$ Fourier modes and $N_T = 40$ Chebyshev polynomials. Error at each location is defined as the absolute difference between the current solution and the reference solution obtained with $N_M = 25$ Fourier modes and $N_T = 100$ Chebyshev polynomials (the reference solution provide machine level accuracy).

$$\|\theta_U(X)\|_\infty = \sup_{0\leqslant X\leqslant 2\pi/\alpha}|\theta(X, y_U(X))| \tag{5.5}$$

as a quantitative measure of the error. This norm is very strict and thus provides an unambiguous means to judge the accuracy of enforcement of boundary conditions. Dependence of boundary error as a function of geometric parameters for a fixed number of Fourier modes N_M is illustrated in Figs. 6 and 7. The reader may note in judging these results that $S = 2$ corresponds to a situation when the lowest extreme of the upper wall touches the lower wall. The available results suggest that the error is at machine accuracy level if α and S are below certain critical values. Once these values are reached, the error begins to increase rapidly in a fairly universal manner. This critical values of α and S can be increased by increasing the number of Fourier modes N_M used in the calculation, but the qualitative character of the error increase remains unchanged.

Distribution of temperature along the upper wall $\theta_U(X)$ over a single spatial period is displayed in Fig. 8. The expected value is zero, however the actual value is different and its magnitude illustrates the error in the enforcement of boundary conditions. This error is oscillatory in X with the maximum occurring around $X = 0$, i.e., around the upper extreme of the deformed wall. The same problem has been solved directly in the fixed

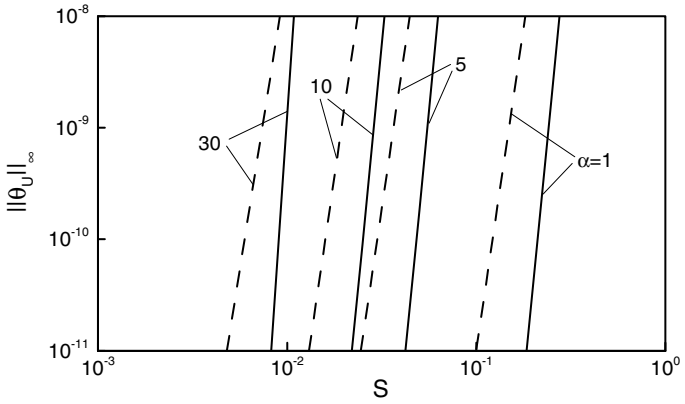

Fig. 6. The $\|\theta_U(X,t)\|_\infty$ norm (see Eq. (5.5)) evaluated using the IBC method as a function of the wave amplitude S for selected values of the wave number α for the model problem (5.3)–(5.4) with $c = \pi$. The dashed and solid lines represent results obtained with the $N_M = 10$, 15 Fourier modes, respectively. The reader may note that $S = 2$ corresponds to the trough of the wave reaching the bottom wall. $N_T = 70$ Chebyshev polynomials were used in the calculations.

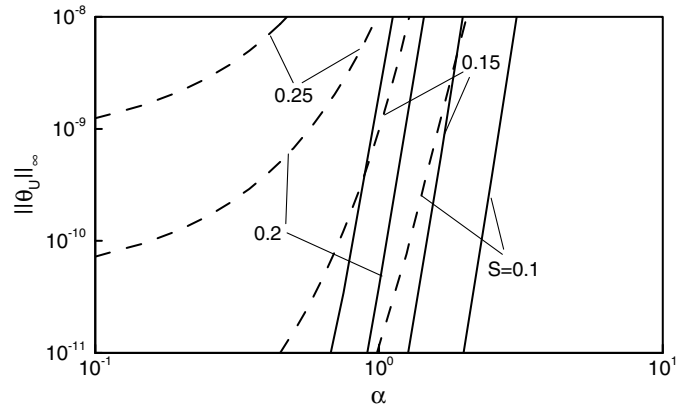

Fig. 7. The $\|\theta_U(X,t)\|_\infty$ norm (see Eq. (5.5)) evaluated using the IBC method as a function of the wave number α for selected values of the wave amplitude S for the model problem (5.3)–(5.4) for $c = \pi$. The dashed and solid lines represent results obtained with the $N_M = 10$, 15 Fourier modes, respectively. The reader may note that $S = 2$ corresponds to the trough of the wave reaching the bottom wall. $N_T = 70$ Chebyshev polynomials were used in the calculations.

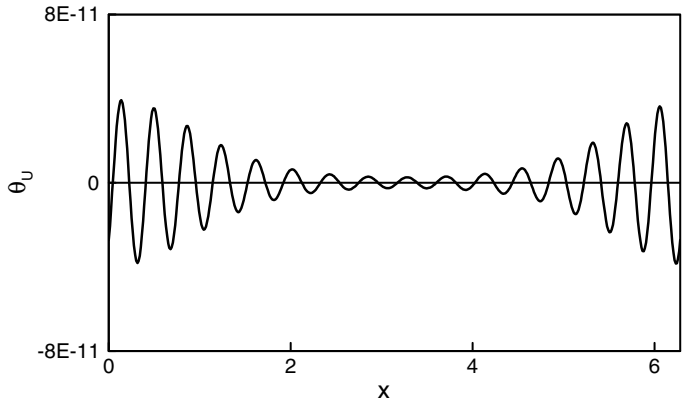

Fig. 8. Distribution of temperature at the upper wall θ_U for the model problem (5.3)–(5.4) with the phase speed $c = \pi$, the amplitude $S = 0.2$ and the wavenumber $\alpha = 1$. The presented results were obtained using the IBC method with $N_M = 15$ Fourier modes and $N_T = 70$ Chebyshev polynomials.

coordinate system as a moving boundary problem and the error variations as a function of time are illustrated in Fig. 9. It can be seen that the magnitude and pattern of distribution of the error remain the same as a function of time, however, the pattern shifts in the direction of the positive x-axis with the phase speed of the wave, i.e., its maximum follows the movement of the upper extreme of the wall.

Fig. 10 illustrates variations of the temperature at a few test points as a function of time over five time periods determined using direct solution of (5.3)–(5.4) in the fixed frame of reference, i.e., solving it as a moving boundary problem. It can be seen that the algorithm faithfully reproduces the oscillatory character of temperature variations and the phase shift between different spatial locations. Fig. 11 illustrates spatial distribution of the heat flux at the upper wall for the same problem as a function of time over one time period. Changes in the variations of the spatial distributions of the heat flux as a function of time demonstrate a correct phase shift. Fig. 12 illustrates variations of the maximum error in the evaluation of the temperature as a function of the temporal step size Δt. The character of these variations demonstrates that the algorithm delivers the first- and second-order accuracy for time simulations, as theoretically predicted.

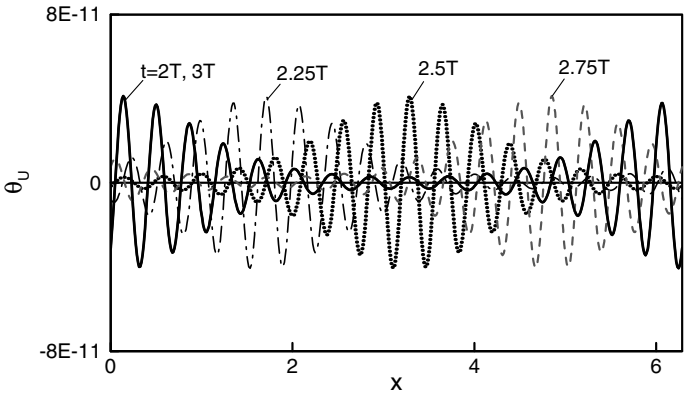

Fig. 9. Distribution of temperature at the upper wall θ_U at $t = 2T$, $2.25T$, $2.5T$, $2.75T$ and $3T$, where T stand for one time period, for the model problem (5.3)–(5.4) with the amplitude $S = 0.2$, the wave number $\alpha = 1.0$ and the phase speed $c = \pi$. The presented results were obtained through a direct solution of the moving boundary problem in the fixed coordinates system (x, y) using the IBC method with $N_M = 15$ Fourier modes and $N_T = 70$ Chebyshev polynomials. Solution corresponding to the fixed boundary problem in the moving frame of reference was used as the initial condition. Presented results correspond to the 3rd period after initiations of the calculations.

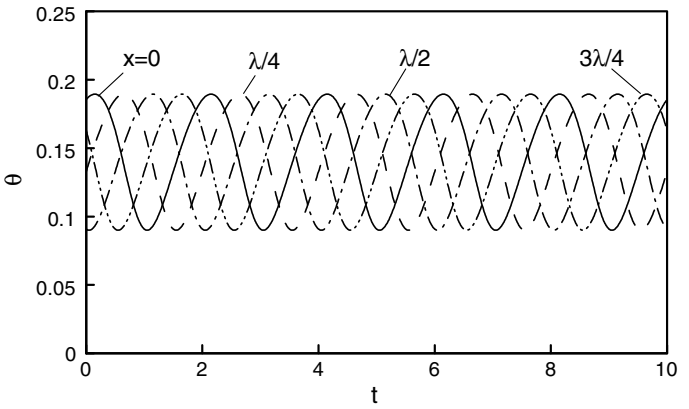

Fig. 10. Variations of the temperature θ at points $(x, y) = (0, 0.7)$, $(\lambda/4, 0.7)$, $(\lambda/2, 0.7)$, $(3\lambda/4, 0.7)$ for the model problem (5.3)–(5.4) with the amplitude $S = 0.15$, the wavenumber $\alpha = 1.0$ and the phase speed $c = \pi$ solved directly as a moving boundary problem in the fixed reference frame for five time periods. Solution of the corresponding fixed boundary problem in the moving frame of reference was used as the initial condition. $N_M = 15$ Fourier modes and $N_T = 70$ Chebyshev polynomials were used in the computations.

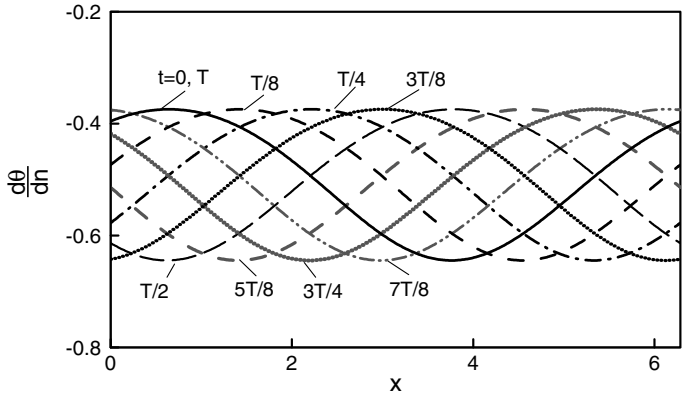

Fig. 11. Variations of heat flux distribution at the upper wall at times $t = 0$, $T/8$, $T/4$, $3T/8$, $T/2$, $5T/8$, $3T/4$, $7T/8$ and T, where T stand for one time period. Other conditions as in Fig. 10.

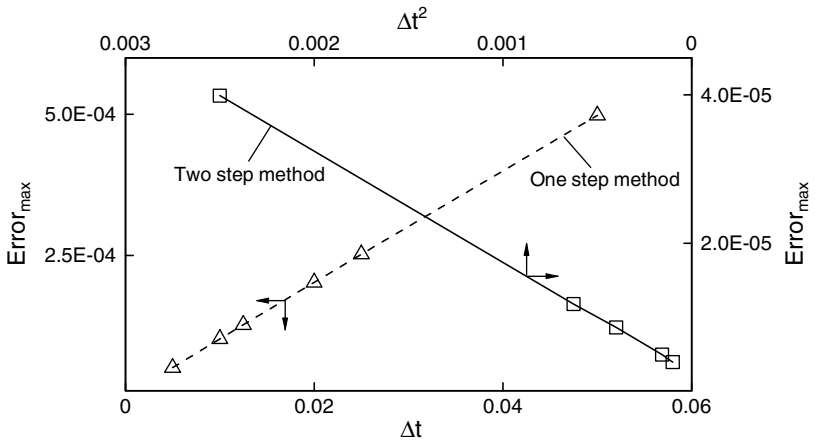

Fig. 12. Variations of the maximum error as a function of the step size Δt used in the temporal discretization in the case of the model problem (5.3)–(5.4) with the amplitude $S = 0.05$, the wave number $\alpha = 1.0$ and the phase speed $c = \pi$. Error is defined as the difference between the results obtained through the direct solution of the moving boundary problem in the fixed frame of reference and the corresponding fixed boundary problem in the moving frame of reference at a time corresponding to $t = 1.0$. $N_M = 10$ Fourier modes and $N_T = 60$ Chebyshev polynomials were used in the computations. Solution of the fixed boundary problem in the moving frame of reference was used as the initial condition for the solution of the moving boundary problem.

5.2. Standing elastic wave

Consider standing elastic wave at the upper wall with the lower wall being flat. The shape of the slot can be described as

$$y_U(x,t) = 1 + S\sin(\alpha x)\cos(\omega t), \quad y_L = -1. \tag{5.6}$$

where α denotes the wave number, S stands for the amplitude and ω denotes the frequency of the wave. Time variations of the shape of the slot are illustrated in Fig. 13. We wish to determine variations of the temperature in the interior of the slot while keeping the temperature of the upper wall at $\theta_U = 0$ and at the lower wall at $\theta_L = 1$. The full test problem has the form

$$-\partial\theta/\partial t + \partial^2\theta/\partial x^2 + \partial^2\theta/\partial y^2 = 0 \tag{5.7}$$

with boundary conditions in the form

$$\theta(x,-1,t) = 1, \quad \theta(x,y_U(x,t),t) = 0 \quad \text{where } y_U = 1 + S\sin(\alpha x)\cos(\omega t). \tag{5.8}$$

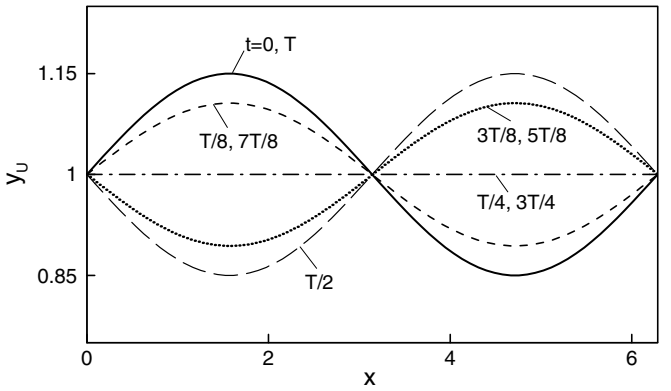

Fig. 13. Shape of the upper wall deformed by elastic standing wave described by Eq. (5.6) with the wavenumber $\alpha = 1.0$, the amplitude $S = 0.15$ and the frequency $\omega = \pi$ at times $t = 0$, $T/8$, $T/4$, $3T/8$, $T/2$, $5T/8$, $3T/4$, $7T/8$ and T, where T denotes one time period.

For convenience, we use the L_∞ norm for θ evaluated at the upper wall defined as

$$\|\theta_U(x,t)\|_\infty = \sup_{0\leqslant X\leqslant 2\pi/\alpha}|\theta(x, y_U(x,t), t)| \tag{5.9}$$

as a quantitative measure of the error. Fig. 14 illustrates variations of the above norm over two time periods with the initial conditions corresponding to the solution of a fixed boundary problem with the shape of the boundaries described by (5.8) at $t = 0$. It can be seen that the error changes periodically in time with the frequency equal to double of the frequency of the standing wave. The maximum of the error occurs at times when the slot opening reaches maximum. The location of the maximum error follows location of the maximum slot opening as illustrated in Fig. 15. The character of the error remains unchanged as a function of time which points to the robustness of the algorithm. The magnitude of the error can be reduced by increasing the number of Fourier modes used in the calculations but its qualitative features remain the same, as illustrated in Fig. 14.

The IBC algorithm enforces zero conditions for only the first N_M Fourier modes. Behavior of the remaining available Fourier modes (for $N_M + 1 < n < N_\theta$) provides an illustration of the error behavior and this is illustrated in Fig. 16. The first N_M Fourier modes are indeed zero and the maximum error is associated with the first neglected mode. As the magnitude of the error is related to the size of the slot opening, this error is expected to be the same every half time period and this is indeed the case, as shown in Fig. 16. The same figure displays error associated with solving the same problem using different sizes of the "computational box" and

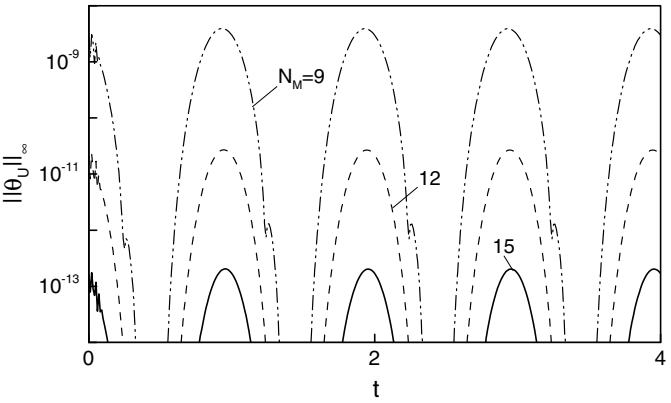

Fig. 14. Variation of the $\|\theta_U(x, t)\|_\infty$ norm as a function of time over two time periods for the model problem (5.7)–(5.8). $N_T = 70$ Chebyshev polynomials were used and the solid, dash and dotted lines corresponds to $N_M = 15$, 12, 9 Fourier modes. Solution of the fixed boundary problem for the geometry described by (5.8) with $t = 0$ was used as an initial conditions. $N_T = 70$. All other conditions are as in Fig. 13.

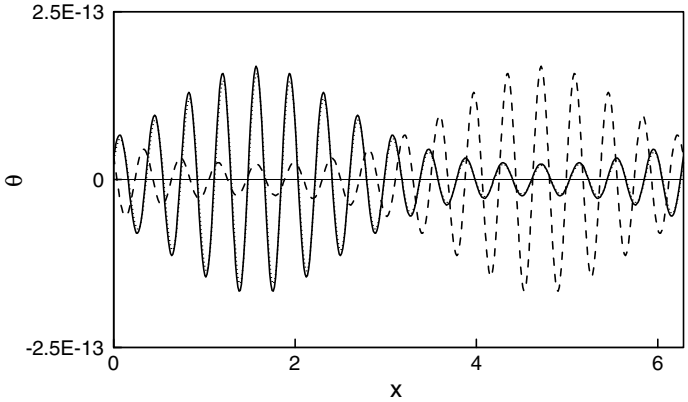

Fig. 15. Distribution of temperature of the upper wall θ_U after three (solid line) and three and half time periods (dashed line) for the model problem (5.7)–(5.8) evaluated using the IBC method with $N_M = 15$ Fourier modes and $N_T = 70$ Chebyshev polynomials. Solution of a fixed boundary problem corresponding to geometry described by Eq. (5.8) with $t = 0$ was used as the initial condition. All other conditions are as in Fig. 13.

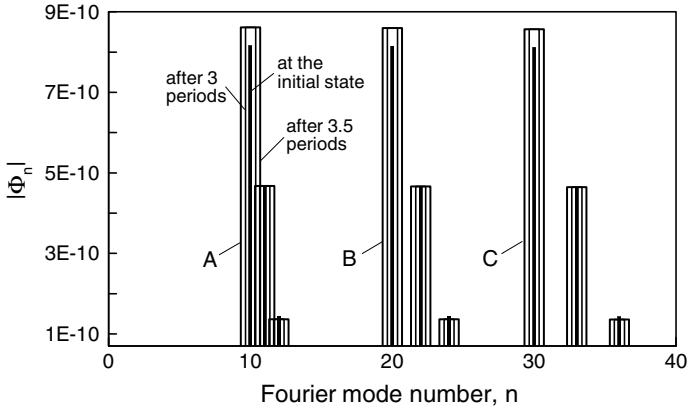

Fig. 16. Fourier spectra of temperature distribution at the upper wall θ_U for the model problem (5.7)–(5.8) with the amplitude $S = 0.15$, the frequency $\omega = \pi$ and the wavelength of the standing wave $\lambda = 2\pi$. The initial conditions correspond to the solution of a fixed boundary problem for the geometry given by (5.8) with $t = 0$. Three different forms of Fourier expansions were considered, i.e., case A: $\alpha = 1.0$, $N_M = 9$; case B: $\alpha = 0.5$, $N_M = 18$ and case C: $\alpha = 1/3$, $N_M = 27$. $N_T = 70$ Chebyshev polynomials used in all cases.

thus using different forms of Fourier expansions. It can be seen that the error is associated with different (but easily predicted) terms of the Fourier expansions and its magnitude does not change. It has been observed that the algorithm does not permit spurious error transfer between different Fourier modes and does not generate any spurious spatial oscillations.

The accuracy of determination of temperature θ in the interior of the slot is dominated by the error associated with the temporal discretization, as the spatial discretization has spectral character and thus is typically much more accurate. Results shown in Fig. 17 demonstrate that the algorithm does deliver the first- and second-order temporal accuracy, as theoretically predicted.

Fig. 18 illustrates time variations of the temperature in the interior of the slot. It can be seen that these variations have strictly periodic character, as expected. The instantaneous isotherms inside a slot deformed by an elastic wave with a more complex shape are illustrated in Fig. 19. The variations of the heat flux at the upper wall for the same slot are illustrated in Fig. 20. These results illustrate the ability of the algorithm to deal with complex movements of the boundaries that require the use of several Fourier modes.

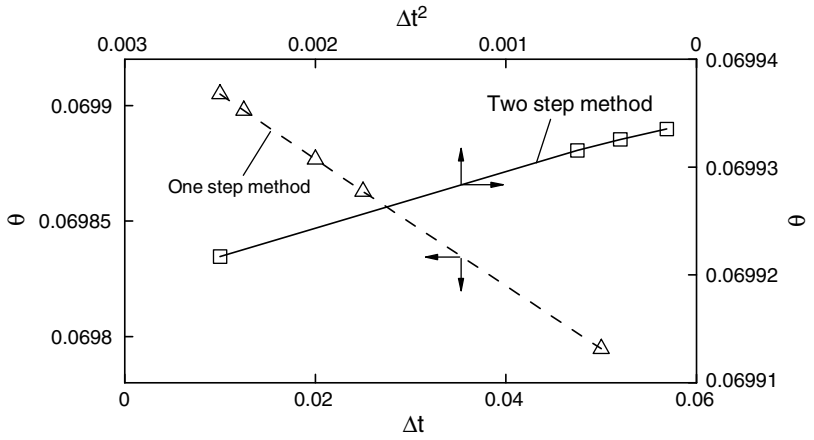

Fig. 17. Variations of temperature θ as a function of the step size Δt at a test point $(x, y) = (3\pi/2, 0.7)$ for the model problem (5.7) and (5.8) with the wave amplitude $S = 0.05$, the wavenumber $\alpha = 1$ and the frequency $\omega = \pi$ at a time $t = T + 1.0$ where T denotes time period. The initial conditions correspond to the solution of a fixed boundary problem for the geometry given by (5.8) with $t = 0$. $N_M = 10$ Fourier modes and $N_T = 60$ Chebyshev polynomials used in the computations.

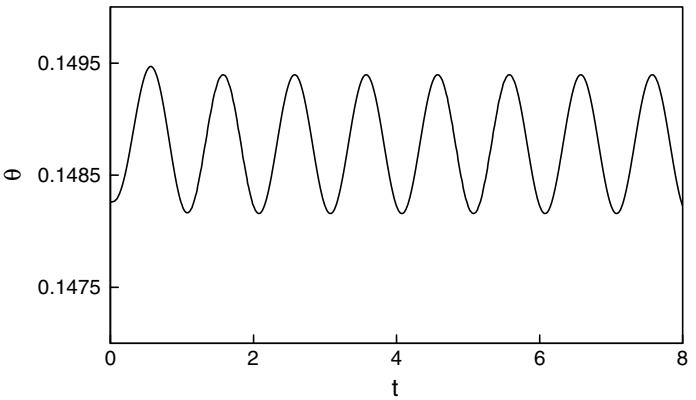

Fig. 18. The evolution of the temperature θ at a test point $(x, y) = (0,0.7)$ during the first four time periods for the model problem (5.7) and (5.8) with the wave properties described in Fig. 13 (starting with solution after one time cycle as the initial condition). The initial conditions correspond to the solution of a fixed boundary problem for the geometry given by (5.8) with $t = 0$. The results were determined using $N_M = 15$ Fourier modes and $N_T = 70$ Chebyshev polynomials.

5.3. Efficiency of the algorithm

Efficiency of the algorithm is dictated by the cost of construction of the matrix of coefficients and solution of the resulting system of linear equations. Both actions have to be repeated at each step of the time-dependent solution process. All tests referred to in the discussion below had been carried out in the MATLAB computing environment using the same hardware.

Structure of the matrix in the case of IBC method has been discussed in Section 3. Entries corresponding to the field equations need to be computed only once at the very beginning of the computations as they remain unchanged. Entries corresponding to the boundary conditions need to be re-computed at each time step as they change due to the movement of the boundaries. On contrary, all entries need to be recomputed at each time step in the DT method. In addition, the cost of a single construction of the coefficient matrix is significantly higher in the case of the DT method due to the presence of numerous and complex coefficients in the equations. The relative advantage of the IBC method is illustrated by noting that in the case of the model

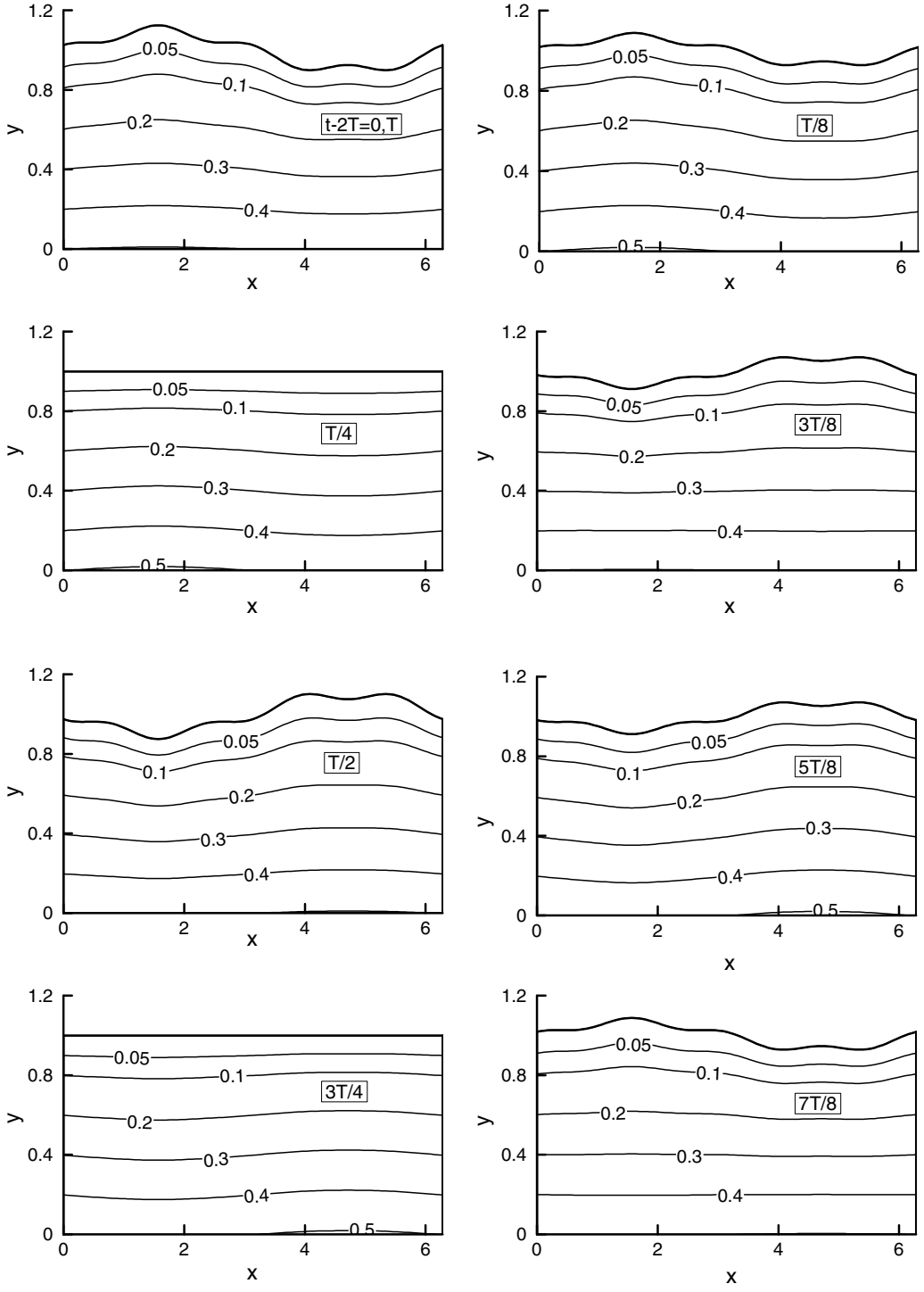

Fig. 19. Instantaneous isotherms in the upper part of a slot bounded by $y_L(x,t) = -1$, $y_U(x,t) = 1 + (-0.05ie^{ix} + 0.0125e^{4ix} + CC)\cos(\omega t)$ for $\omega = \pi$ using $N_M = 15$ and $N_T = 70$ evaluated after two time periods at times $t - 2T = 0$, $T/8$, $T/4$, $3T/8$, $T/2$, $5T/8$, $3T/4$, $7T/8$ and T, where T stands for one time period and CC is the abbreviation for complex conjugate. The initial conditions correspond to the solution of a fixed boundary problem in a slot with geometry given by the above equation with $t = 0$.

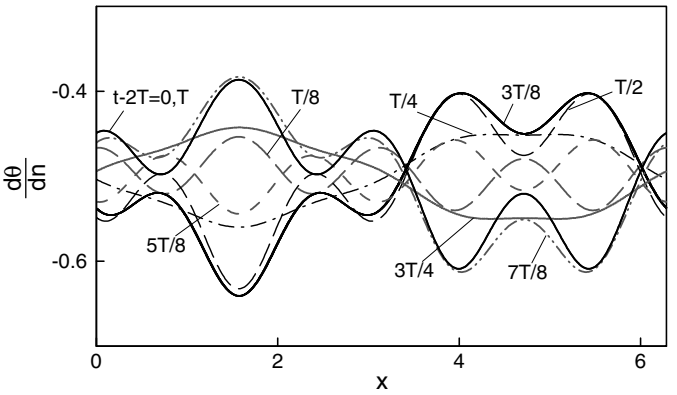

Fig. 20. Variations of heat flux distribution at the upper wall in a slot with the flat lower wall $y_L(x, t) = -1$ and a standing elastic wave in the form $y_U(x, t) = 1 + (-0.5Sie^{izx} + 0.125Se^{4izx} + CC)\cos(\omega t)$ with $S = 0.1, \alpha = 1.0$ and $\omega = \pi$ at the upper wall at times $t - 2T = 0$, $T/8$, $T/4$, $3T/8$, $T/2$, $5T/8$, $3T/4$, $7T/8$ and T, where T stands for one time period and CC is the abbreviation for complex conjugate. The initial conditions correspond to the solution of a fixed boundary problem for the geometry corresponding to the shape of the slot at time $t = 0$. The results were determined using $N_M = 15$ Fourier modes and $N_T = 70$ Chebyshev polynomials.

problem (5.7)–(5.8) with $N_M = 15$ Fourier modes and $N_T = 70$ Chebyshev polynomials, it took 592 s to construct a complete matrix in the case of DT method, but only about 8 s in the IBC method. The latter is significantly reduced at the next time step, while the former has to be entirely repeated, which adds to the relative advantage of the IBC method. For this reason the development of the DTM method has not been pursued.

Once constructed, the solution of the system of linear equations can be carried out using standard methods resulting in a direct algorithm, as discussed in Section 3. Since the coefficient matrix in the DT method is full, no savings associated with special features of the matrix can be expected. Matrix in the case of IBC method has a special structure and this provides opportunity to use iterative algorithm. The performance of different iterative/decoupled schemes is illustrated in Table 1 and compared with the direct algorithm. Since the overall accuracy of the time-dependent solution is determined by the error of the temporal discretization, the convergence criterion for the decoupled algorithms in these tests had been set at 10^{-5}. The performance of the decoupled algorithm can be improved by taking advantage of the information available at the previous time step and re-arranging the iteration strategy. Three different strategies have been tested. Version A has been described in Section 3, version B uses extrapolated values of the modal functions during the first iteration and continues iterations until convergence criteria are met and version C uses only extrapolated values of the modal functions and eliminates iterations. In all cases the method remains second-order accurate as the extrapolation provides second-order accuracy in time. The results (see Table 1) show significant savings resulting from the use of iterative/decoupled algorithms as compared with the direct algorithm. The distinction between different iterative algorithms and their limitations are illustrated in Table 2. The cost of the direct algorithm remains the same regardless of the magnitude of amplitude S of the standing wave. The cost of version A of the iterative algorithm increases as the amplitude S increase and, for sufficiently high value of S the algorithm diverges. Versions B and C behave in a similar manner but diverge for smaller values of S. The relative performances of different versions of the iterative algorithm are very similar, and they all require less

Table 1
Time requirements for the direct and various iterative/decoupled schemes for the IBC algorithm for the model problem (5.7)–(5.8) with $S = 0.1$, $\alpha = 1.0$, $\omega = \pi$ and $N_T = 70$

Number of Fourier modes, N_M	Time required for 100 time steps (in s)			
	Direct algorithm	Decoupled algorithm		
		Version A	Version B	Version C
10	299.8508	34.7997	32.9297	29.1454
15	880.6996	86.5740	84.3365	83.2125

Table 2
Time requirement for the direct and various iterative/decoupled schemes for the IBC algorithm for the model problem (5.7)–(5.8) with $\alpha = 1.0$, $\omega = \pi$, $N_M = 15$ and $N_T = 70$ for various level of wave amplitude

Wave amplitude, S	Time required for 100 time steps (in seconds)			
	Direct algorithm	Decoupled algorithm		
		Version A	Version B	Version C
0.05	880.0006	84.5860	83.2216	83.1216
0.10	880.6996	86.5740	84.3365	83.2125
0.15	879.6771	94.3541	88.3559	Diverges
0.20	880.2463	104.4011	110.3439	Diverges
0.25	880.2125	156.8901	Diverges	Diverges
0.30	880.2829	Diverges	Diverges	Diverges
0.35	880.4658	Diverges	Diverges	Diverges

All other conditions are same as Table 1.

computer time as compared with the direct algorithm by an order of magnitude. The direct algorithm however provides access to much larger amplitudes of boundary motions.

6. Conclusions

We have developed a fully-implicit, spectrally-accurate algorithm for moving boundary problems using immersed boundary conditions concept. Computations are carried out using a fixed computational domain where the field equations are discretized using a combination of Fourier and Chebyshev expansions. Boundary of the physical domain moves through the computational domain and its location is tracked using the concept of immersed boundary conditions, i.e., the boundary conditions are replaced by constraints that enforce physical conditions along lines internal to the solution domain. The algorithm provides sharp resolution of the location of the moving boundary similar to the case of algorithms based on mapping methods where one of the coordinate lines overlap with the moving boundary. The computational cost of the algorithm is significantly smaller as compared with the mapping-based algorithms because the part of the coefficient matrix that corresponds to the field equations needs to be constructed only once and only entries corresponding to boundary conditions need to be recomputed at each time step. The coefficient matrix has special structure that provides opportunities for the use of much more efficient iterative solution methods. These methods can reduce the overall computational cost by an order of magnitude as compared to the direct method, however, they limit the ability of the algorithm to handle large-amplitude motions of the boundaries. Such algorithms remain of interest nevertheless as they can be easily parallelized and require less memory.

Acknowledgements

This work has been carried out with support of SHARCNET and NSERC of Canada. SHARCNET of Canada provided computing resources. The preliminary version of this work has been presented during the 15th Annual Conference of the Computational Fluid Dynamics Society of Canada, Toronto, Ontario, May 27–31, 2007.

Appendix A

Temporal discretization of (3.6) using a one-step implicit method results in

$$[\Gamma^2 D^2 - (n^2\alpha^2 + \Delta t^{-1})]\Phi^{(n)}_{\tau+1} = -\Delta t^{-1}\Phi^{(n)}_{\tau}, \quad n \in \langle 0, N_M\rangle.$$

Temporal discretization of (4.2) using the same method results in

$$D^2\Psi^{(n)}_{\tau+1} + \sum_{s=-N_M}^{N_M}[w^{(n-s)}_{1,\tau+1} + \mathrm{i}s\alpha w^{(n-s)}_{2,\tau+1}]D\Psi^{(s)}_{\tau+1} - \sum_{s=-N_M}^{N_M}[(s\alpha)^2 + \Delta t^{-1}]w^{(n-s)}_{3,\tau+1}\Psi^{(s)}_{\tau+1} = -\Delta t^{-1}\sum_{s=-N_M}^{N_M} w^{(n-s)}_{3,\tau}\Psi^{(s)}_{\tau}, \quad n \in \langle 0, N_M\rangle.$$

Appendix B

Expressions required in Eq. (4.2):

$$\eta_t = [(y_L)_t(\eta-1) - (y_U)_t(\eta+1)]/(y_U - y_L),$$
$$\eta_x = [(y_L)_\xi(\eta-1) - (y_U)_\xi(\eta+1)]/(y_U - y_L),$$
$$\eta_{xx} = \frac{\eta(y_U - y_L)[(y_L)_\xi - (y_U)_\xi][(y_L)_{\xi\xi} - (y_U)_{\xi\xi}] + 2y_L(y_U)_{\xi\xi} - 2y_U(y_L)_{\xi\xi}}{(y_U - y_L)^2} + \frac{-2\eta[(y_U)_\xi - (y_L)_\xi]^2 + 2[(y_U)_\xi^2 - (y_L)_\xi^2]}{(y_U - y_L)^2},$$
$$\eta_y = \frac{2}{y_U - y_L},$$

where subscripts ξ, t denote derivative $\mathrm{d}/\mathrm{d}\xi$, $\mathrm{d}/\mathrm{d}t$, respectively.

References

[1] J.M. Floryan, H. Rasmussen, Numerical analysis of viscous flows with free surfaces, Appl. Mech. Rev. 42 (1989) 323.
[2] J. Glimm, J.W. Grove, X.L. Li, K.M. Shyue, Y. Zeng, Q. Zhang, Three-dimensional front tracking, SIAM J. Sci. Comput. 19 (1998) 703.
[3] F.H. Harlow, J.E. Welch, Numerical study of large amplitude free surface motions, Phys. Fluids 9 (1966) 842.
[4] C.W. Hirt, B.D. Nichols, Volume of fluid (VOF) method for the dynamics of free boundaries, J. Comput. Phys. 39 (1981) 201.
[5] S.Z. Husain, J.M. Floryan, Immersed boundary conditions method for unsteady flow problems described by the Laplace operator, Expert Systems in Fluid Dynamics Research Laboratory Report ESFD-1/2006, Department of Mechanical and Materials Engineering, The University of Western Ontario, London, Ontario, N6A 5B9, Canada, 2006.
[6] J.M. Hyman, Numerical methods for tracking of interfaces, Physica D 12 (1984) 396.
[7] L. Kogut, The influence of surface topography on the electromechanical characteristics of parallel-plate capacitors, J. Micromech. Microeng. 15 (2005) 1068.
[8] R. Mittal, G. Iaccarino, Immersed boundary methods, Annu. Rev. Fluid Mech. 37 (2005) 239.
[9] S.J. Osher, J.A. Sethian, Fronts propagating with curvature dependent speed: algorithms based on Hamilton–Jacobi formulations, J. Comp. Phys. 79 (1988) 12.
[10] C.S. Peskin, The fluid dynamics of heart valves: experimental, theoretical and computational methods, Annu. Rev. Fluid Mech. 14 (1982) 235.
[11] J. Szumbarski, J.M. Floryan, A direct spectral method for determination of flows over corrugated boundaries, J. Comp. Phys. 153 (1999) 378.
[12] R. Scardovelli, S. Zaleski, Direct numerical simulation of free surface and interfacial flow, Annu Rev. Fluid Mech. 31 (1999) 567.
[13] J.A. Sethian, P. Smereka, Level set methods for fluid interfaces, Annu. Rev. Fluid Mech. 35 (2003) 341.